This is an open access article published under a Creative Commons Attribution (CC-BY) License, which permits unrestricted use, distribution and reproduction in any medium, provided the author and source are cited.

ACS AUTHORCHOICE

ACS OMEGA

http://pubs.acs.org/journal/acsodf

Article

Influence of Mineral Composition of Chars Derived by Hydrothermal Carbonization on Sorption Behavior of CO_2, CH_4, and O_2

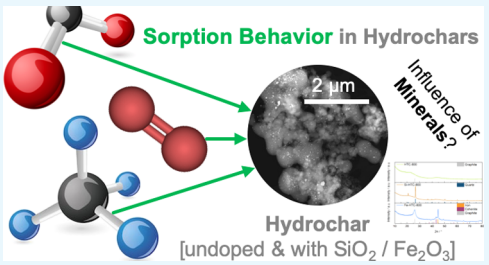
Carsten Wedler, Katrin Lotz, Arash Arami-Niya, Gongkui Xiao, Roland Span, Martin Muhler, Eric F. May, and Markus Richter*

Cite This: *ACS Omega* 2020, 5, 10704−10714

Read Online

ACCESS | Metrics & More | Article Recommendations | Supporting Information

ABSTRACT: The doping of SiO_2 and Fe_2O_3 into hydrochars that were produced by the hydrothermal carbonization of cellulose was studied with respect to its impact on the resulting surface characteristics and sorption behavior of CO_2, CH_4, and O_2. During pyrolysis, the structural order of the Fe-doped char changed, as the fraction of highly ordered domains increased, which was not observed for the undoped and Si-doped chars. The Si doping had no apparent influence on the oxidation temperature of the hydrochar in contrast to the Fe-doped char where the oxidation temperature was reduced because of the catalytic effect of Fe. Both dopants reduced the micro-, meso- and macroporous surface areas of the chars, although the Fe-doped chars had larger meso- and macroporosity than the Si-doped char. However, the increased degree in the structural order of the carbon matrix of the Fe-doped char reduced its microporosity relative to the Si-doped char. The adsorption of CO_2 and CH_4 on the chars at temperatures between 273.15 and 423.15 K and at pressures up to 115 kPa was slightly inhibited by the Si doping but strongly suppressed by the Fe doping. For O_2, however, the Si doping promoted the observed adsorption capacity, while Fe doping also showed an inhibiting effect.



1. INTRODUCTION

Hydrothermal carbonization (HTC) chars, which are pyrolyzed hydrochars derived via hydrothermal carbonization under high pressure from lignocellulosic biomass and water, have aroused interest in many fields of science and application over recent years.[1] One promising research focus is the use of hydrochars as a fuel in biomass-fired power generation or as a possible substitute in coal-fired power plants[2,3] because such an application could help meet increasing global energy demand while reducing associated CO_2 emissions. After pyrolysis, the resulting HTC chars possess large surface areas, which make them also a promising adsorbent material for subsequent use in the removal of environmental pollutants from flue gases or waste water.[4]

The elemental composition of solid biofuels can differ a lot. Depending on different raw plants, woods, or agricultural wastes, the mineral content of, e.g., iron, silica, or potassium can vary significantly, which can have a catalytic effect on morphology, pyrolysis, gasification, and combustion.[5−8] Trubetskaya et al.[6] have shown for two biomasses with different silica and potassium content that the high silica content of rice husk leads to a preserved shape of the char particles during pyrolysis, whereby the low silica and high potassium content of wheat straw lead to a broader deviation of particle shapes. The higher potassium content of the wheat straw also resulted in a higher reactivity of the char, which was also confirmed by various studies for different biomasses.[5,9,10] Khelfa et al.[7] have shown the catalytic effect of Fe_2O_3 on pyrolysis and gasification of miscanthus chars. For these studies, the catalytic effect was shown using different natural biomasses with different mineral compositions[6] by the addition of further mineral particles to the biomass particles[7] or by acid leaching of most of the original mineral content with additional doping of the investigated mineral.[5,8−10] Therefore, interactions between the different mineral components or influences of the acid leaching cannot be distinguished clearly.

Due to the rudimental composition of the hydrochar derived via HTC from pure cellulose, interactions between different minerals can be excluded. By doping minerals into the hydrochar matrix, the nature and the arrangement of active sites on the surface of the char can be modified, which leads to different combustion and adsorption properties. The doping of iron oxide into the hydrochar results as well in a faster oxidation of the char due to the catalytic effects of iron,[11−13] whereas the doping of silica does not show a significant effect on the oxidation rate.[12] As diffusion and adsorption precede oxidation, this observation suggests that such doping might similarly influence these mass transport mechanisms. Any differences in the diffusion and adsorption of gas molecules in

Received: December 19, 2019
Accepted: April 8, 2020
Published: May 8, 2020



© 2020 American Chemical Society

https://dx.doi.org/10.1021/acsomega.9b04370
ACS Omega 2020, 5, 10704−10714

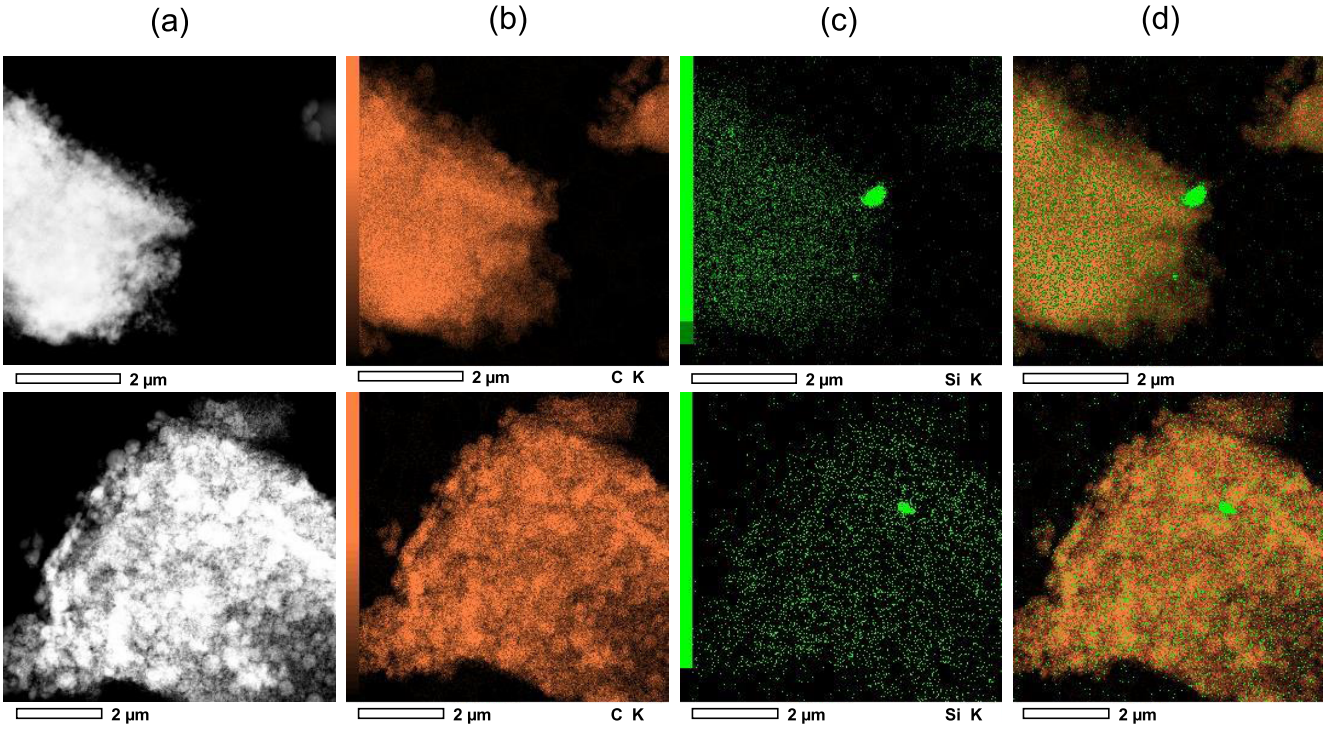


Figure 1. Scanning transmission electron microscopy (STEM) micrograph (a) and elemental mapping with respect to carbon (b) and silicon (c) for two different particles of the Si-doped char. The overlay (d) is based on the individual distributions of carbon and silicon.

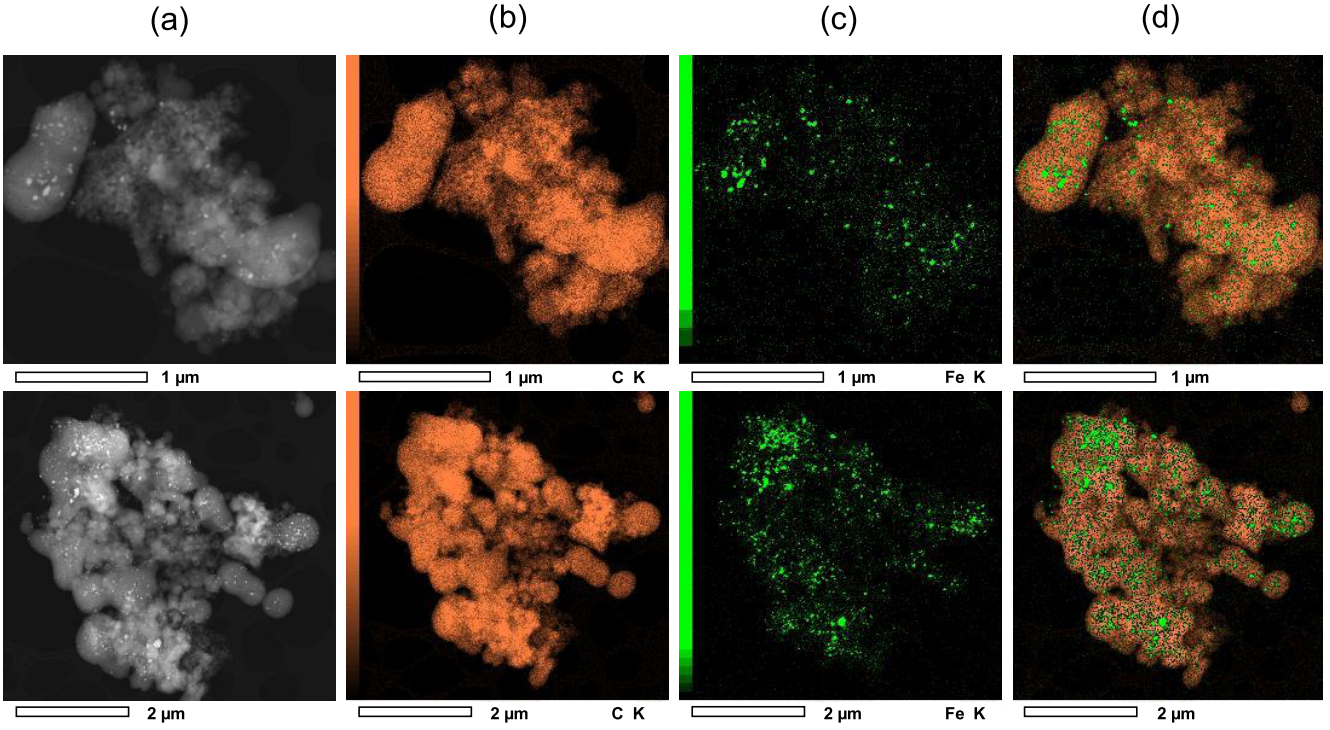


Figure 2. STEM micrograph (a) and elemental mapping with respect to carbon (b) and iron (c) for two different particles of the Fe-doped char. The overlay (d) is based on the individual distributions of carbon and iron.

the porous structure of the char would also lead to changed reaction rates during combustion and gasification given the importance of the these mass transport mechanisms to such reactions.[14] Several studies investigated the adsorption behavior of HTC chars, originating from different biomass materials such as different wood and agricultural residues.[15−19]

Since the biomasses consist of various amounts of cellulose, minerals, and functional groups, a closer look on those components is herein expedient as well. Very few studies focusing on the influence of the mineral content or the functional groups of the hydrochars on the adsorption properties have been carried out. Yu et al. investigated the

https://dx.doi.org/10.1021/acsomega.9b04370
ACS Omega 2020, 5, 10704−10714

influence of the iron content of hydrochars on the removal of estrogen, and Lei et al. studied the influence of the nitrogen-containing functional groups on the removal of chromium, both from waste water.[20,21] To the best of our knowledge, no study exists on the influence of the iron or silica content on the adsorption of CO_2, CH_4, or O_2.

Therefore, a novel approach towards the influence of iron and silica doping on the adsorption behavior of CO_2, CH_4, and O_2 is presented in this study, followed by a comprehensive estimation of the volumetric adsorption measurement uncertainty. Changes in morphology and the amount of active surface sites due to mineral doping and pyrolysis of the hydrochars lead to different adsorption behavior of the chars. Since the adsorbed phase is a precursor for the following solid−gas interactions during pyrolysis, gasification, and combustion, the investigation of the influence of the mineral composition leads to a better understanding of the process.

2. RESULTS AND DISCUSSION

2.1. Characterization of the HTC Chars. *2.1.1. Elemental Mapping.* Electron microscopy imaging and energy-dispersive elemental mapping of the doped HTC chars were performed to obtain information about the mode of incorporation of the dopants and are presented in Figures 1 and 2. According to the micrographs, the particles consist of agglomerates of spheres differing in size. Elemental mapping of the Si-doped (see Figure 1b−d) and Fe-doped (see Figure 2b−d) HTC char reveals that the dopant particles are in immediate vicinity of the carbonaceous spheres. Thus, we assume that the dopant particles are incorporated into the hydrochar during the hydrothermal carbonization process and remain in contact with the char matrix after pyrolysis. For the Fe-doped char, elemental mapping shows a higher dispersion of the dopant in the char, which is presumably due to the lower particle size of the added Fe_2O_3 particles compared to those of SiO_2.

2.1.2. X-ray Diffraction (XRD). To identify the phases of organic and inorganic matter in the HTC chars, XRD patterns were recorded and are shown in Figure 3. Also shown are the peak locations corresponding to the reference patterns of graphite, quartz, iron, and cohenite.

In the XRD pattern of the undoped char, no sharp reflections can be observed in the range 2θ = 10−80°, suggesting that this carbon material is X-ray amorphous. TEM imaging of the char verifies a low degree of structural order (see Figure S1 in the Supporting Information). Thus, pyrolysis up to T = 1073 K does not generate a high fraction of highly ordered domains in the undoped HTC char. The XRD pattern of the Si-doped HTC char contains several sharp reflections, which can be assigned to quartz (SiO_2). This indicates that the dopant maintains its phase composition during the hydrothermal synthesis and the subsequent pyrolysis. In contrast, a phase transition occurs for the Fe-doped char: carbothermal reduction of the Fe_2O_3 dopant during the thermal treatment results in metallic iron (Fe^0) and iron carbide (Fe_3C), as revealed by the detail investigations shown previously.[22] This is possibly accompanied by an increase in the structural order of the carbonaceous matter, as indicated by the reflection at 2θ = 26° referring to graphitic carbon. Given that any structural order is much less pronounced for the undoped and the Si-doped char, the diffraction pattern and the TEM image (see Figure S1 in the Supporting Information) reveal that the in situ addition of the iron dopant introduces structural order to the char by enabling far more highly ordered domains than observed in the other chars.

2.1.3. Surface Area Characteristics and Pore Size Distribution (PSD). For all three HTC chars, the meso- to macroporous surface area was investigated by conducting a BET analysis of sorption isotherms measured for N_2 at T = 77.36 K (Figure 4). For all HTC chars, a pronounced increase

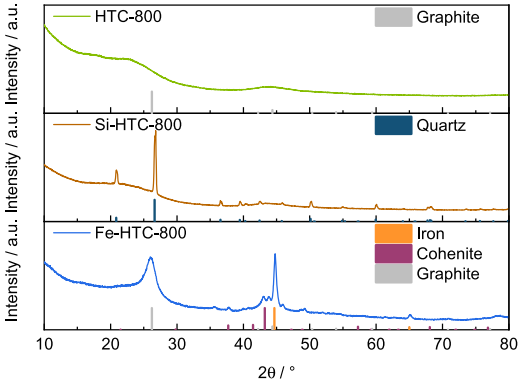


Figure 3. XRD patterns of the undoped (HTC-800), Si-doped (Si-HTC-800), and Fe-doped (Fe-HTC-800) HTC char (reference patterns: graphite: 01-075-1621; SiO_2: 01-070-7344; Fe^0: 03-065-4899; Fe_3C: 01-089-2005).

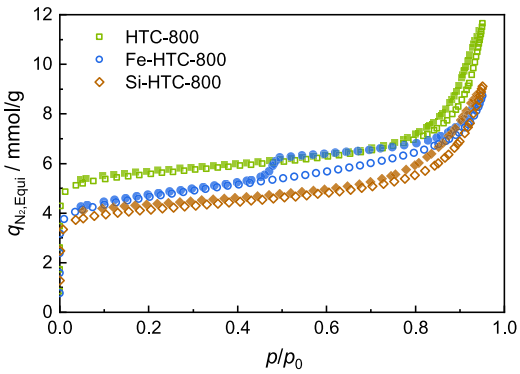


Figure 4. N_2 physisorption isotherms at T = 77.36 K of the undoped (HTC-800), Si-doped (Si-HTC-800), and Fe-doped (Fe-HTC-800) HTC chars. Hollow symbols correspond to adsorption data, while filled symbols correspond to desorption data.

in the amount of N_2 adsorbed is observed for very low relative pressures, which gives a first hint of the more microporous carbon structures. For p/p_0, in the range 0.1−0.8, the doped chars exhibit reduced adsorption capacity, suggesting a low fraction of small mesopores relative to the undoped char. Stronger adsorption occurs as the saturation pressure is approached, with capillary condensation evident in large mesopores and macropores.

Although the shape of the sorption isotherms of the undoped and Si-doped char are similar, the amount of N_2 adsorbed on the latter is significantly lower. This is reflected by the Brunauer−Emmett−Teller (BET) surface areas of the chars, which amounted to 416, 350, and 310 m^2/g for the undoped, Fe-doped, and Si-doped HTC char, respectively (see Table 1). In contrast to the undoped and the Si-doped chars, the adsorption and desorption isotherms of the Fe-doped char exhibit a more pronounced hysteresis. On the basis of previous studies,[22] this feature is presumably caused by the desorption

https://dx.doi.org/10.1021/acsomega.9b04370
ACS Omega 2020, 5, 10704−10714

Table 1. Comparison of Surface Areas of the Undoped (HTC-800), the Si-Doped (Si-HTC-800) and the Fe-Doped (Fe-HTC-800) HTC Chars Determined by N_2 Adsorption at T = 77.36 K (BET) and by CO_2 Adsorption at T = 273.15 K (DA and BET)

	HTC-800	Si-HTC-800	Fe-HTC-800
$S_{N_2,BET}$ [m^2/g]	416	310	350
$S_{CO_2,DA}$ [m^2/g]	784	666	502
$S_{CO_2,BET}$ [m^2/g]	357	341	236

of the adsorbate from cavities in the carbonaceous material produced by the structural changes occurring during pyrolysis. The increase for all three samples at very small pore sizes below 2 nm indicates a pronounced micropore structure.

To investigate the micropore structure (<2 nm), CO_2 adsorption isotherm data at T = 273.15 K (see Figure 7) were used to determine a micropore surface area of each char (see Table 1) via the Dubinin–Astakhov equation, as extended by the equation of Medek.[23,24] In general, the micropore surface area of all three chars is significantly larger than the BET surface area. We note that comparisons of the absolute values obtained from the models should be treated with caution, although differences in both $S_{N_2,BET}$ and $S_{CO_2,DA}$ are likely indicative of the HTC chars having different pore structures. The micropore surface area of the Si-doped char (666 m^2/g) is much larger than that of the Fe-doped char (502 m^2/g), which possibly reflects the reduction in microporosity caused by the generation of highly ordered domains induced by iron doping. In a few literature studies,[25,26] the BET theory has also been applied to the CO_2 isotherm data to calculate another estimate of the microporous surface area, $S_{CO_2,BET}$. This is done here, and the results presented in Table 1 also indicate that Fe-HTC-800 has the smallest surface area.

By conducting NLDFT calculations using the data from the initial slope of the N_2 adsorption isotherm, the pore size distribution (PSD) of the three chars for the micropore regime was calculated (see Figure 5). For all three chars, the regularization parameter of λ = 1.625 was applied based on the optimized result of the L-curve for the Si-doped HTC char. For the undoped and Si-doped char, a bimodal distribution was obtained, with a sharp peak at around 0.4 nm for both and a broader peak at around 0.9 nm for the undoped and around 1.2 nm for the Si-doped char. Having in mind that N_2 is kinetically hindered at cryogenic temperatures to diffuse into the narrow micropores, the absolute values of the pore size distribution have to be considered carefully but give at least a hint of the distribution of the micropores. The larger peak areas of the undoped char show a more pronounced microporous structure than those of the Si-doped chars. A unimodal distribution with a broad peak around 0.8 nm was obtained for the Fe-doped char, resulting in a less pronounced microporosity for the Fe-doped char. These observations confirm the results of the microporous surface area $S_{CO_2,DA}$. The unimodality also indicates a different structural order of the Fe-doped char, as described in Section 2.1.2.

2.1.4. Oxidation Behavior. The stability of the HTC chars can be determined by temperature-programmed oxidation (TPO), as the conversion of carbon materials by oxidation usually occurs at lower temperatures than required for gasification. The differential thermogravimetric (DTG) curves shown in Figure 6 were calculated by evaluating the first derivative of the sample mass changes measured during the TPO experiments.

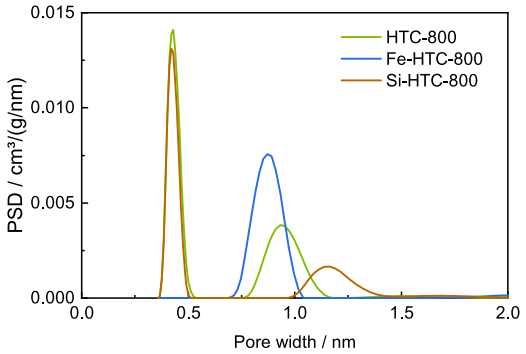


Figure 5. Pore size distributions obtained by nonlinear density functional theory (NLDFT) analysis of the undoped (HTC-800), Si-doped (Si-HTC-800), and Fe-doped (Fe-HTC-800) HTC char.

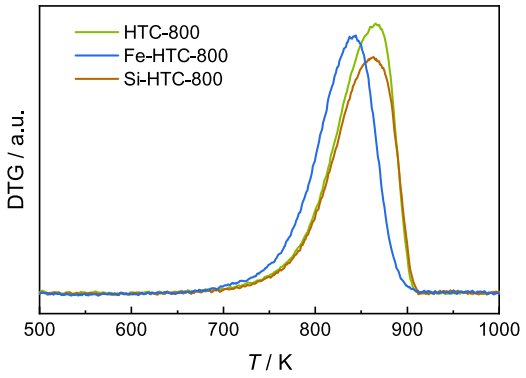


Figure 6. DTG curves during TPO in synthetic air in a thermobalance of the undoped (HTC-800), Si-doped (Si-HTC-800), and Fe-doped (Fe-HTC-800) HTC char.

The DTG profiles of the three HTC chars exhibit one broad signal in the temperature range between 673.15 and 923.15 K, corresponding to a single-step mass loss. The oxidation temperature corresponding to the maximum of the DTG peak was T = 865.15 K for the undoped char and was not affected by the addition of SiO_2. The decreased height of the DTG signal obtained for the Si-doped char is caused by the lower relative fraction of oxidizable carbonaceous material present relative to that in the same initial amount of undoped char. Doping with iron produced a slight decrease of the char oxidation temperature, which can be attributed to the catalytic effect of the dopant. Nevertheless, the TPO and DTG data reveal that all three HTC chars are stable at the temperatures at which the sorption of CO_2, CH_4, and O_2 were measured.

2.2. Sorption Equilibria of CO_2, CH_4, and O_2. The adsorption loadings of CO_2 on the three different chars were measured at five temperatures between 273.15 and 423.15 K and are shown in Figure 7. For each temperature, similar trends can be observed. The largest CO_2 loadings were measured at p = 115 kPa for the undoped char (3.46 mmol/g at T = 273.15 K to 0.38 mmol/g at T = 423.15 K), followed by the Si-doped char (3.06 mmol/g at T = 273.15 K to 0.34 mmol/g at T = 423.15 K) and the Fe-doped char (2.24 mmol/g at T = 273.15 K to 0.24 mmol/g at T = 423.15 K).

The large adsorption loading of the undoped char can be explained by the fact that it had the largest BET surface area

https://dx.doi.org/10.1021/acsomega.9b04370
ACS Omega 2020, 5, 10704−10714

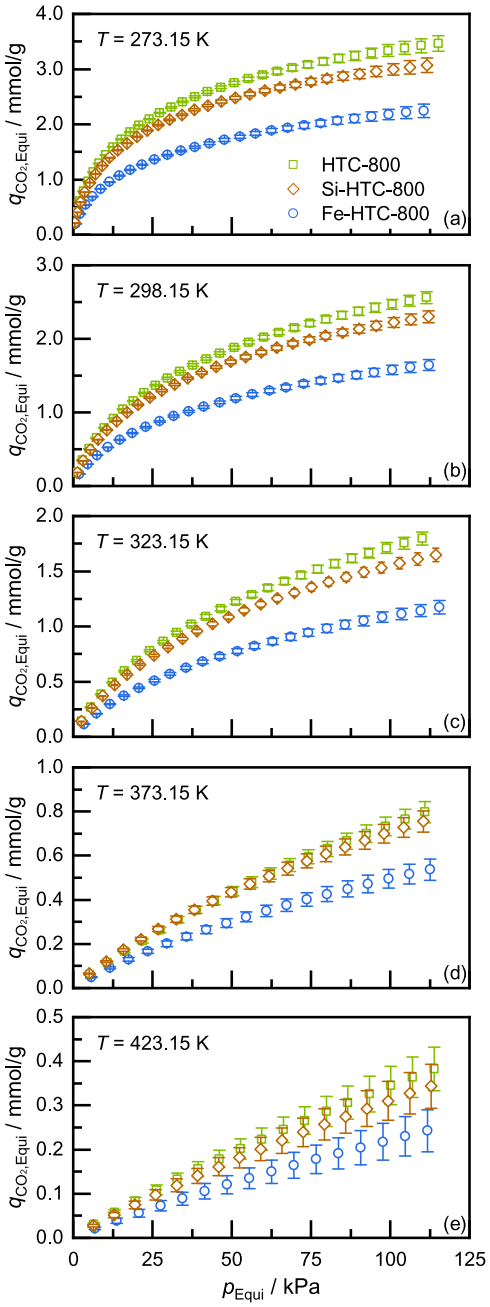


Figure 7. Adsorption loadings of CO_2 on the undoped (HTC-800), Si-doped (Si-HTC-800), and Fe-doped (Fe-HTC-800) HTC chars at different temperatures. (a) T = 273.15 K; (b) T = 298.15 K; (c) T = 323.15 K; (d) T = 373.15 K; and (e) T = 423.15 K. The isotherms for the undoped HTC char at T = 273.15 and 298.15 K were reported previously.[27]

(416 m^2/g) and/or as a result of the reduction in attractive forces between the CO_2 and carbonaceous material caused by the doped minerals. However, the lower CO_2 loading of the Fe-doped char relative to the Si-doped char cannot be related to their BET surface areas of 350 and 310 m^2/g, respectively. However, the different microporous pore structure of the Fe-doped char (see Section 2.1.3) resulting from the enhanced structural order likely impedes the CO_2 adsorption process. A similar trend for the different chars was obtained for the adsorption measurements with CH_4 at the four temperatures between 273.15 and 373.15 K, although the adsorption loadings were considerably lower than for CO_2 (see Figure 8). At 1.80, 1.62, and 1.15 mmol/g for the undoped, Si-doped,

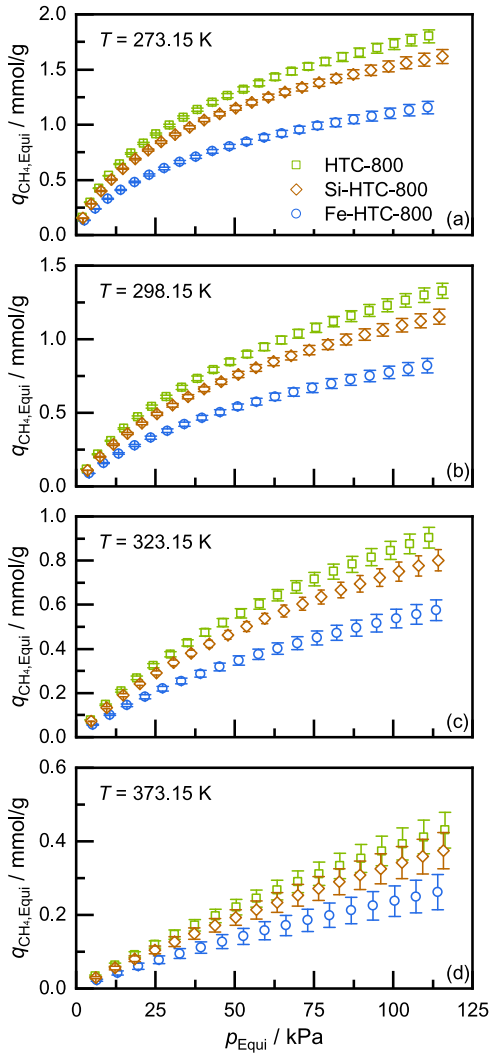


Figure 8. Adsorption loadings of CH_4 on the undoped (HTC-800), Si-doped (Si-HTC-800), and Fe-doped (Fe-HTC-800) HTC chars at different temperatures. (a) T = 273.15 K; (b) T = 298.15 K; (c) T = 323.15 K; (d) T = 373.15 K. The isotherms for the undoped HTC char at 273.15 and 298.15 K were reported previously.[27]

and Fe-doped chars, respectively, the resulting adsorption loadings at p = 115 kPa and T = 273.15 are all about 48% lower than that for CO_2. This trend simply reflects the generally lower adsorption affinity of CH_4 on any material (see here for another example[28]). The difference in adsorption loadings for the three chars can also be explained in terms of the changes in microporosity resulting from the doping process, since the adsorption of CH_4 is related to the microporosity as well.[29] However, a directly inhibiting effect of the doped minerals is also possible.

Figure 9 shows the adsorption of O_2 on the chars at T = 273.15 and 298.15 K, which exhibit a different trend than that observed for CO_2 and CH_4. At T = 273.15 K, the largest O_2 loadings were measured for the Si-doped char (0.81 mmol/g), followed by the undoped char (0.78 mmol/g) and the Fe-doped char (0.47 mmol/g): this sequence cannot be explained by either the microporosity or the meso- to macroporosity of the samples. Furthermore, for the Si-doped char, a repeatable

https://dx.doi.org/10.1021/acsomega.9b04370
ACS Omega 2020, 5, 10704−10714

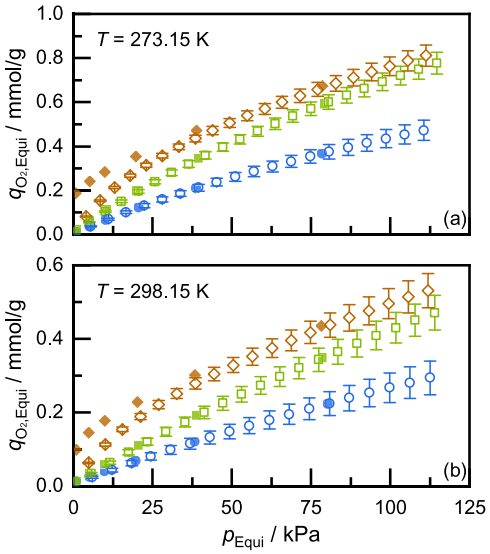


Figure 9. Adsorption and desorption loadings of O_2 on the undoped (HTC-800), Si-doped (Si-HTC-800), and Fe-doped (Fe-HTC-800) HTC chars at (a) T = 273.15 K and (b) T = 298.15 K. Adsorption plotted by empty and desorption by filled markers.

desorption hysteresis was observed for the lowest pressures at both temperatures, which indicates a behavior other than regular physisorption. To explain this behavior, it is helpful to consider the XRD patterns of the Si-doped char, which show the presence of quartz. At the temperature of the doping process of T = 473.15 K, the crystalline structure of the doped SiO_2 is α-quartz.[30] Above a temperature of T = 846 K, a displacive transformation between α-quartz and β-quartz occurs, whereby one of the tetrahedra rotates slightly with a resulting decrease in density of SiO_2.[30] During the pyrolysis of the Si-doped char at a temperature of 1073 K, the quartz structure should thus change to β-quartz but change back to α-quartz during the subsequent cooling. Some parts of the crystalline structure may be preserved in a so-called paramorph state of the β-quartz. The chemisorption of O_2 on β-quartz has been reported,[31] so we hypothesize that hysteresis observed in this work may reflect the presence of this β-quartz paramorph in the Si-doped char. However, we have no proof for this hypothesis and further verification is necessary but during several adsorption cycles with the same sample, this desorption hysteresis was found to be reproducible.

To summarize the inhibiting effect of the iron doping on the char adsorption behavior, loadings for each of the three gases at T = 298.15 K with regard to the absolute mass of carbon in the chars are shown in Figure 10. For CO_2 and CH_4, the adsorption loadings on the undoped and the Si-doped chars are essentially the same, while the adsorption on the Fe-doped char is much lower, reflecting a clear inhibiting effect by the dopant. For the case of O_2, the promoting effect of silica can also be observed.

3. CONCLUSIONS

To understand the catalytic influence of minerals in chars, a combined approach to investigate changes of char morphology and adsorption behavior of mineral-doped HTC chars is presented. Different characteristics (XRD, BET, DA, and TPO) and the adsorption behavior (CO_2, CH_4, and O_2 at temperatures between T = 273.15 and 423.15 K) of an undoped, a Si-doped, and a Fe-doped char were investigated.

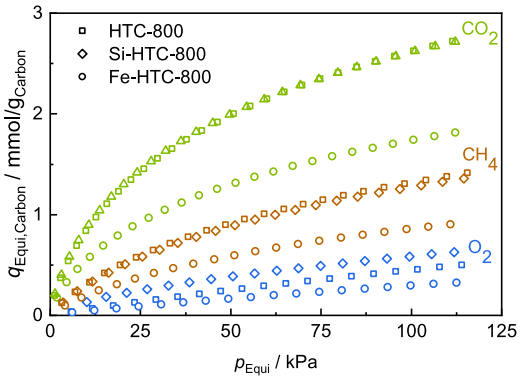


Figure 10. Adsorption loadings of the three gases at T = 298.15 K for the undoped (HTC-800), Si-doped (Si-HTC-800), and Fe-doped (Fe-HTC-800) HTC char.

The XRD patterns and TEM images show that the Fe doping increases the structural ordering of the char during pyrolysis while the Si doping had no apparent effect on the char structure. BET analysis (N_2 adsorption at T = 77.36 K) and Dubinin–Astakhov analysis (CO_2 adsorption at T = 273.15 K) showed that the doped chars had smaller macro- and micropore surface areas than that of the undoped char. While the Fe-doped char had a larger macropore surface area than that of the Si-doped char, the opposite was true for the micropore surface areas as a result of the higher fraction of highly ordered domains in the Fe-doped char.

For the first time, the influence of mineral doping on the gas adsorption behavior of HTC chars was investigated. The highest adsorption loadings for CO_2 and CH_4 were observed for the undoped char, reflecting its higher microporosity, followed by the Si-doped and Fe-doped chars. For O_2 adsorption, the highest adsorption affinity was observed for the Si-doped char, which may be explained by chemisorption of O_2 on a paramorph of the doped quartz. Due to less adsorption of all three analysis gases on the Fe-doped char, it can be concluded that Fe doping and the resulting increase in structural order during subsequent pyrolysis leads to less accessible adsorption sites on the surface of the char. The catalytic effect of iron on char conversion is therefore not a consequence of a higher concentration of adsorption sites on the surface. For future research work, the effect of the mineral influence on the rate of pore diffusion has also to be taken into account to reach a complete understanding of the influence on mass transfer.

4. EXPERIMENTAL METHODS

4.1. Synthesis of Hydrochars. Doped synthetic chars were prepared by hydrothermal carbonization (HTC) using cellulose as a precursor followed by pyrolysis of the obtained hydrochars.[32] In situ doping with SiO_2 or Fe_2O_3 imitated the incorporation of minerals into coal during the natural coalification process.[12]

For the hydrothermal synthesis, a 50 mL polytetrafluoroethylene inliner of a stainless steel autoclave was applied to the reactor. For the undoped hydrochar, 6 g of α-cellulose (Sigma-Aldrich, BioReagent) was suspended within 30 mL of deionized H_2O. In situ doping was performed by the addition of either 5 wt % Fe_2O_3 (Alfa Aesar, 20–40 nm) or 5 wt % SiO_2 (Riedel-de Haën, 40–63 μm) to the cellulose dispersion. The loaded autoclave was heated in a convection oven to T =

https://dx.doi.org/10.1021/acsomega.9b04370
ACS Omega 2020, 5, 10704–10714

473.15 K, which generated an autogenous pressure of about 1.55 MPa inside the autoclave. After 24 h, the autoclave was cooled to room temperature. Subsequently, the yielded suspension was filtered and the resulting solid was washed with deionized H_2O until a neutral pH was reached. The obtained hydrochar was dried in a convection oven at T = 378.15 K for 24 h. Afterwards, the hydrochar was loaded into a quartz boat, which was placed in a horizontal oven and pyrolyzed in a N_2 flow (Air Liquide; purity: 99.999 mol %) by heating at a linear rate of 5 K/min to T = 1073.15 K, which was then held for 2 h. The resulting undoped, Si-doped, and Fe-doped chars are labeled HTC-800, Si-HTC-800, and Fe-HTC-800, respectively.

An overview of the composition of the synthesized and pyrolyzed chars is presented in Table 2. Pyrolysis causes the release of volatiles, resulting in an increase of the carbon content accompanied by a decrease of the H and O content in the remaining char. For the undoped char, the degree of carbonization was higher than 90 wt %. To specify the extent to which the added dopants were incorporated, the actual loadings are reported as a weight percentage of the particular metal component in the char. The doped amounts correspond to 2.7 wt % Si content for the Si-doped char and 3.8 wt % Fe content for the Fe-doped char. A proximate analysis revealed that the undoped char contained no mineral components in contrast to the doped chars.

Table 2. Overview of Characterization of the Undoped (HTC-800), Si-Doped (Si-HTC-800), and Fe-Doped (Fe-HTC-800) HTC Char by Elemental Analysis, AAS, and Proximate Analysis

	HTC-800	Si-HTC-800	Fe-HTC-800
C [wt %]	94.1	84.7	90.6
H [wt %]	0.6	0.8	0.6
O [wt %]	5.3	11.9	5.0
Fe [wt %]			3.8
Si [wt %]		2.7	
volatiles [wt %]	4	4	4
ash [wt %]	0	8	7

4.2. Characterization of Chars. The prepared chars were characterized with respect to composition, structural properties, and reactivity in an oxidative atmosphere. A vario Micro cube (Elementar Analysensysteme) was used for elemental (CHNS) analysis of the chars. The amount of Si and Fe included in the Si-doped and the Fe-doped char, respectively, was determined by atomic absorption spectroscopy (AAS). For electron microscopy imaging, the doped HTC chars were first suspended in a mixture of ethanol and water and then dispersed in an ultrasonic bath. Afterwards, the samples were placed on an Au grid with a lacey carbon film. Scanning transmission electron microscopy (STEM) and energy-dispersive X-ray (EDX) spectroscopy were performed using a JEOL JEM-2800 microscope. The X-ray diffraction patterns in the 2θ range of 5−80° for Cu Kα radiation were recorded by an Empyrean diffractometer (PANalytical) at the Department of Mineralogy at Ruhr University Bochum. Phase identification was based on reference patterns by the International Center for Diffraction Data (ICDD), a HighScore Plus software (Malvern Panalytical). The volatile and ash fractions in the chars were derived from thermogravimetric measurements using a magnetic-suspension balance (TA Instruments, previously Rubotherm) with a coupled quadrupole mass spectrometer (Thermostar, Pfeiffer Vacuum). For proximate analysis, about 30 mg of the carbon materials was heated under a He flow of 100 cm^3/min (Air Liquide; purity: 99.999 mol %) to a temperature of 1173.15 K with a heating rate of 10 K/min followed by a treatment at T = 1088.15 K in a 100 cm^3/min flow of 20/80 vol % O_2/He (Air Liquide; purities: 99.995, 99.999 mol %). The oxygen content of the chars was calculated by subtraction: O (wt %) = 100 (wt %) − C (wt %) − H (wt %) − Si (wt %) − Fe (wt %). The influence of dopants on the stability of the chars was evaluated by temperature-programmed oxidation (TPO) experiments in the magnetic-suspension balance. During TPO, about 30 mg of the chars was heated at 5 K/min to T = 1173.15 K in a 100 cm^3/min flow of 20/80 vol % O_2/He.

To determine the meso- to macroporous surface area according to the theory of Brunauer, Emmett, and Teller (BET),[33] N_2 (Air Liquide; purity: 99.999 mol %) adsorption measurements at T = 77.36 K were carried out in a BELSORP-mini (BEL Japan). Before conducting the adsorption measurements, the samples were degassed for 6 h at a temperature of T = 473.15 K. However, at cryogenic temperatures, the diffusion of N_2 into the HTC char's narrow micropores is highly restricted and a quantitative analysis of the sample's microporosity cannot be often achieved by such measurements.[34,35]

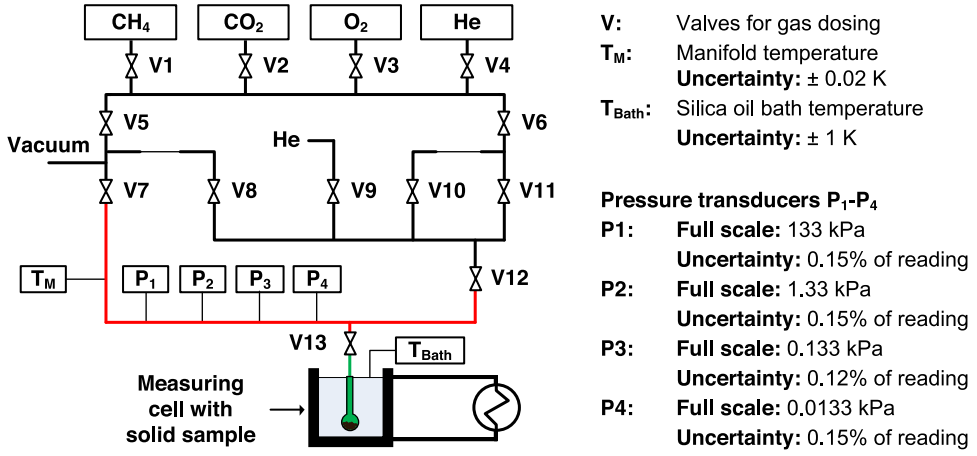


Figure 11. Schematic of the volumetric measurement system.

https://dx.doi.org/10.1021/acsomega.9b04370
ACS Omega 2020, 5, 10704−10714

Table 3. Compressibility Factor Z Calculated for T and p_{equi} = 0.1 MPa

	Z					
	77.36 K	273.15 K	298.15 K	323.15 K	373.15 K	423.15 K
CO_2		0.99335	0.99502	0.99620	0.99768	0.99853
He		1.00053	1.00048	1.00044	1.00037	1.00032
CH_4		0.99764	0.99827	0.99873	0.99932	
O_2		0.99904	0.99936			
N_2	0.95747					

Table 4. Nonideality Factor α for T and p_{equi} = 0.1 MPa[a]

	α (10^{-9}/Pa)					
	77.36 K	273.15 K	298.15 K	323.15 K	373.15 K	423.15 K
CO_2		−66.522	−49.793	−38.069	−23.249	−14.699
He		5.2618	4.7785	4.3688	3.7138	3.2151
CH_4		−23.561	−17.299	−12.737	−6.7668	
O_2		−9.5601	−6.3854			
N_2	−425.29					

[a]Note that the ASAP 2020 device requires a different definition of α in 1/Torr.

Instead, using CO_2 as the adsorbate at T = 273.15 K, this kinetic restriction can be avoided, and given the saturation pressure for CO_2 at this temperature is 3.4851 MPa,[36] the initial stage of physisorption can be studied at moderate pressures in the range 0.1−100 kPa.[34] However, as CO_2 has a quadrupole moment that can interact with functional groups on the char's surface, this could in principle influence the pore filling. Nevertheless, most carbonaceous surfaces in general do not contain as many functional groups as, e.g., zeolites or MOFs. Furthermore, Lotz et al. observed a strong loss of functional groups on the hydrochars during pyrolysis. Accordingly, CO_2 was used in this work to analyze the microporous structure of the chars[22,34] using the Dubinin−Astakhov theory with the extended equation by Medek.[23,24] For the CO_2 sorption experiments, the volumetric system described in Section 4.3 was used.

The N_2 adsorption data was also used to calculate the pore size distribution by nonlinear density functional theory (NLDFT) calculations. The 2D-NLDFT model for porous carbons with heterogeneous surfaces was used,[37,38] which is implemented in the analysis software SAIEUS by Micromeritics.

4.3. Sorption Experiments with CO_2, CH_4, and O_2. For the adsorption investigations, a volumetric measurement system (model ASAP 2020 by Micromeritics) was used, which was slightly modified from its previous configurations, as shown in Figure 11.[39−43] The temperature of the solid sample in the measurement cell (marked green in Figure 11) was controlled by a homemade heating jacket filled with a thermostated heat transfer oil. Temperature and pressure in the manifold volume (marked red in Figure 11) were measured continuously using transducers with full scales and uncertainties shown in Figure 11. After degassing the solid sample at T = 473.15 K, the manifold volume was filled with gas up to a certain pressure (e.g., 5, 10 kPa). Subsequently, valve V13 was opened, allowing gas to flow into the measuring cell and the pressure change associated with adsorption to be determined; after reaching a steady state pressure, the process was repeated multiple times up the isotherm. CO_2, O_2, CH_4, and He were supplied by Coregas with a purity of 99.995 mol %.

4.3.1. Experimental Procedure. For clarity and to promote a better understanding of the following uncertainty estimation, we briefly present the working equations of the volumetric sorption measurement system. The adsorbed amount at equilibrium is obtained by calculating the difference between the dosed amount n_{dosed} and the amount of gas in the free space n_{FS} inside the measuring volume.

$$n_{equi,i} = n_{dosed,i} - n_{FS,i} \tag{1}$$

The cumulative nature of the measurement requires that the amounts dosed during previous pressure steps have to be accounted for when evaluating $n_{dosed,i}$. The amount previously dosed is incremented by the difference between the initial and equilibrium amounts of gas inside the manifold volume V_M (marked red in Figure 11). The real gas behavior is considered using the nonideality factor α (see eq 4).

$$n_{dosed,i} = n_{dosed,i-1} + \frac{p_{intial} \cdot V_M}{R \cdot T_{M,initial}(1 + \alpha \cdot p_{initial})} - \frac{p_{equi} \cdot V_M}{R \cdot T_{M,equi}(1 + \alpha \cdot p_{equi})} \tag{2}$$

Before starting the adsorption measurement, the free gas volume in the measuring volume (marked green in Figure 11) is determined twice by helium pycnometry, once at the measurement temperature set by the bath ($V_{F,bath}$, T_{bath}) and once at room temperature ($V_{F,room}$, T_{room}).

$$n_{FS,i} = \frac{p_{equi} \cdot V_{F,bath}}{R \cdot T_{STD}(1 + \alpha \cdot p_{equi})} + \frac{p_{equi}\left(V_{F,bath} - V_{F,room} \cdot \frac{T_{bath}}{T_{room}}\right)}{R \cdot T_{STD}(1 + \alpha \cdot p_{equi})} \tag{3}$$

The standard temperature is defined at T_{STD} = 273.15 K and the nonideality factor is related to the compressibility factor Z, as given in eq 4, which depends on the actual temperature and pressure of the gas.[44] The values[45,46] for the nonideality factor still widely used in sorption science are often traceable to the suggestions of Emmett and Brunauer[47] from 1937. In this work, the far more accurate reference equations of state for CO_2,[36] He,[48] CH_4,[49] O_2,[50] and N_2[51] were used to calculate Z

https://dx.doi.org/10.1021/acsomega.9b04370
ACS Omega 2020, 5, 10704−10714

for different temperatures, using the software package Trend 4.0.[52] Hence, the calculated values for Z and α are listed in Tables 3 and 4, respectively. These tables also indicate at which temperature the measurements with the different gases were conducted. CO_2 was measured from T = 273.15 K up to T = 423.15 K, while CH_4 and O_2 were only measured up to T = 373.15 and T = 298.15 K, respectively. At higher temperatures, the experimental loadings of CH_4 and O_2 were so small that they could not be reproduced properly.

$$\alpha = \frac{Z(T_{bath}, p_{equi}) - 1}{p_{equi}} \quad (4)$$

The adsorption capacity can finally be obtained through the ratio of the adsorbed amount of molecules and the mass of the sample loaded into the measuring cell.

$$q_i = \frac{n_{equi,i}}{m_{sample}} \quad (5)$$

4.3.2. Estimation of the Volumetric Adsorption Measurement Uncertainty. The measurement uncertainty was estimated according to the "Guide of the Expression of Uncertainty in Measurements", abbreviated as GUM.[53] The combined standard uncertainty u_c of the adsorption capacity q_i can be calculated by eq 6 for every single pressure step. Due to the cumulative nature of the measurements, the uncertainties of all previous pressure steps j have to be considered for the uncertainty of the pressure step i (j defined from 1 to i). In Table 5, the standard uncertainties of the different contributions are listed. The standard uncertainties of the pressure and temperature measurements as well of the sample mass determination are taken from the manufacturer specifications. For the volumes, no specifications were provided by the manufacturer of the volumetric measurement system and so we conservatively estimated these values. The sensitivity coefficients $\partial q_i/\partial x$ were determined by conducting a sensitivity analysis, whereby the influence of the standard uncertainties on the adsorption loading q_i was evaluated. Using a coverage factor of k = 2, the combined expanded uncertainty $U_c(q_i)$ in determination of adsorption capacity can be calculated; values are indicated in the figures of Section 2.2, and the numerical values are provided as state point uncertainties in the tables of the Supporting Information.

Table 5. Uncertainty Budget for the Relative Combined Standard Uncertainty in Adsorption Loading $u_c(q_i)/q_i$[a]

uncertainty contribution	standard uncertainty	contribution to $u_c(q_i)/q_i$
equilibrium pressure $p_{equi,i}$	1.5×10^{-5} p	2.34×10^{-3}
initial pressure $p_{initial,i}$	1.5×10^{-5} p	2.21×10^{-3}
manifold volume V_M	1×10^{-3} V_M[b]	1.45×10^{-6}
free volume at room temperature $V_{F,room}$	2×10^{-2} $V_{F,room}$[c]	9.70×10^{-8}
free volume at bath temperature $V_{F,bath}$	2×10^{-2} $V_{F,bath}$[c]	9.35×10^{-3}
bath temperature T_{bath}	0.5 K	9.53×10^{-10}
room temperature T_{room}	0.5 K	1.49×10^{-9}
manifold temperature T_M	0.02 K	2.94×10^{-4}
compressibility factor Z	$(0.02-0.1) \times 10^{-3} Z$[d]	3.94×10^{-9}
mass of sample m_{sample}	0.0005 g	5.57×10^{-6}
$u_c(q_i)/q_i$		1.42×10^{-2}

[a]As an example, the contributions to $u_c(q_i)/q_i$ were calculated for the adsorption of CO_2 on Si-HTC-800 at T = 373.15 K and p = 110.4 kPa. [b]Manifold volume was provided by the manufacturer but not the standard uncertainty. Therefore, standard uncertainty was conservatively estimated. [c]Free volumes were determined by helium pycnometry before the adsorption measurement started. Since the apparatus routine does not provide the values to recalculate those volumes, standard uncertainties were conservatively estimated. [d]The uncertainty depends on the used EOS for the different fluids.[36,48−51]

$$u_c(q_i) = \left[\sum_{j=1}^{i} \left\{ \left(\left(\frac{\partial q_i}{\partial p_{equi,j}} \right) u(p_{equi,j}) \right)^2 + \left(\left(\frac{\partial q_i}{\partial p_{initial,j}} \right) u(p_{initial,j}) \right)^2 \right\} + \left(\left(\frac{\partial q_i}{\partial V_M} \right) u(V_M) \right)^2 + \left(\left(\frac{\partial q_i}{\partial V_{F,room}} \right) u(V_{F,room}) \right)^2 + \left(\left(\frac{\partial q_i}{\partial V_{F,bath}} \right) u(V_{F,bath}) \right)^2 + \left(\left(\frac{\partial q_i}{\partial T_{bath}} \right) u(T_{bath}) \right)^2 + \left(\left(\frac{\partial q_i}{\partial T_{room}} \right) u(T_{room}) \right)^2 + \left(\left(\frac{\partial q_i}{\partial T_M} \right) u(T_M) \right)^2 + \left(\left(\frac{\partial q_i}{\partial Z} \right) u(Z) \right)^2 + \left(\left(\frac{\partial q_i}{\partial m_{sample}} \right) u(m_{sample}) \right)^2 \right]^{0.5} \quad (6)$$

■ ASSOCIATED CONTENT

Supporting Information

The Supporting Information is available free of charge at https://pubs.acs.org/doi/10.1021/acsomega.9b04370.

TEM micrographs of the undoped and Fe-doped HTC char, adsorption loadings and their combined expanded uncertainty of CO_2, CH_4, and O_2 on HTC-800, Si-HTC-800, and Fe-HTC-800 at temperatures between 273.15 and 423.15 K (PDF)

■ AUTHOR INFORMATION

Corresponding Author

Markus Richter − *Applied Thermodynamics, Chemnitz University of Technology, 09126 Chemnitz, Germany; Fluid Science & Resources Division, Department of Chemical Engineering, The University of Western Australia, Perth, WA 6009, Australia;* orcid.org/0000-0001-8120-5646; Phone: +49-371-531-38050; Email: m.richter@mb.tu-chemnitz.de

Authors

Carsten Wedler − *Thermodynamics, Ruhr University Bochum, 44780 Bochum, Germany*

Katrin Lotz − *Laboratory of Industrial Chemistry, Ruhr University Bochum, 44780 Bochum, Germany*

Arash Arami-Niya − *Fluid Science & Resources Division, Department of Chemical Engineering, The University of Western Australia, Perth, WA 6009, Australia; Discipline of Chemical*

https://dx.doi.org/10.1021/acsomega.9b04370
ACS Omega 2020, 5, 10704−10714

Engineering, Western Australian School of Mines: Minerals, Energy and Chemical Engineering, Curtin University, Perth, WA 6845, Australia; orcid.org/0000-0001-6450-0774

Gongkui Xiao − *Fluid Science & Resources Division, Department of Chemical Engineering, The University of Western Australia, Perth, WA 6009, Australia;* orcid.org/0000-0001-9659-6969

Roland Span − *Thermodynamics, Ruhr University Bochum, 44780 Bochum, Germany*

Martin Muhler − *Laboratory of Industrial Chemistry, Ruhr University Bochum, 44780 Bochum, Germany;* orcid.org/0000-0001-5343-6922

Eric F. May − *Fluid Science & Resources Division, Department of Chemical Engineering, The University of Western Australia, Perth, WA 6009, Australia;* orcid.org/0000-0001-5472-6921

Complete contact information is available at: https://pubs.acs.org/10.1021/acsomega.9b04370

Notes

The authors declare no competing financial interest.

■ ACKNOWLEDGMENTS

This work was funded by the Deutsche Forschungsgemeinschaft (DFG, German Research Foundation)—Projektnummer 215035359—TRR 129.

■ REFERENCES

(1) Kambo, H. S.; Dutta, A. A comparative review of biochar and hydrochar in terms of production, physico-chemical properties and applications. *Renewable Sustainable Energy Rev.* **2015**, *45*, 359−378.

(2) Reza, M. T.; Andert, J.; Wirth, B.; Busch, D.; Pielert, J.; Lynam, J. G.; Mumme, J. Hydrothermal Carbonization of Biomass for Energy and Crop Production. *Appl. Bioenergy* **2014**, *1*, 11−29.

(3) Liu, Z.; Balasubramanian, R. Upgrading of waste biomass by hydrothermal carbonization (HTC) and low temperature pyrolysis (LTP): A comparative evaluation. *Appl. Energy* **2014**, *114*, 857−864.

(4) Titirici, M.-M.; White, R. J.; Falco, C.; Sevilla, M. Black perspectives for a green future: hydrothermal carbons for environment protection and energy storage. *Energy Environ. Sci.* **2012**, *5*, 6796.

(5) Jones, J. M.; Darvell, L. I.; Bridgeman, T. G.; Pourkashanian, M.; Williams, A. An investigation of the thermal and catalytic behaviour of potassium in biomass combustion. *Proc. Combust. Inst.* **2007**, *31*, 1955−1963.

(6) Trubetskaya, A.; Jensen, P. A.; Jensen, A. D.; Steibel, M.; Spliethoff, H.; Glarborg, P.; Larsen, F. H. Comparison of high temperature chars of wheat straw and rice husk with respect to chemistry, morphology and reactivity. *Biomass Bioenergy* **2016**, *86*, 76−87.

(7) Khelfa, A.; Sharypov, V.; Finqueneisel, G.; Weber, J. V. Catalytic pyrolysis and gasification of Miscanthus Giganteus: Haematite (Fe2O3) a versatile catalyst. *J. Anal. Appl. Pyrolysis* **2009**, *84*, 84−88.

(8) Farrow, T. S.; Sun, C.; Snape, C. E. Impact of biomass char on coal char burn-out under air and oxy-fuel conditions. *Fuel* **2013**, *114*, 128−134.

(9) Eom, I.-Y.; Kim, J.-Y.; Kim, T.-S.; Lee, S.-M.; Choi, D.; Choi, I.-G.; Choi, J.-W. Effect of essential inorganic metals on primary thermal degradation of lignocellulosic biomass. *Bioresour. Technol.* **2012**, *104*, 687−694.

(10) Perander, M.; DeMartini, N.; Brink, A.; Kramb, J.; Karlström, O.; Hemming, J.; Moilanen, A.; Konttinen, J.; Hupa, M. Catalytic effect of Ca and K on CO 2 gasification of spruce wood char. *Fuel* **2015**, *150*, 464−472.

(11) Lotz, K.; Berger, C. M.; Muhler, M. Catalytic effect of iron phases on the oxidation of cellulose-derived synthetic char. *Energy Procedia* **2019**, *158*, 694−699.

(12) Düdder, H.; Wütscher, A.; Vorobiev, N.; Schiemann, M.; Scherer, V.; Muhler, M. Oxidation characteristics of a cellulose-derived hydrochar in thermogravimetric and laminar flow burner experiments. *Fuel Process. Technol.* **2016**, *148*, 85−90.

(13) Düdder, H.; Lotz, K.; Wütscher, A.; Muhler, M. The influence of iron oxide on the oxidation kinetics of synthetic char derived from thermogravimetric analysis and fixed-bed experiments under isothermal and temperature-programmed conditions. *Fuel* **2017**, *201*, 99−104.

(14) Wedler, C.; Richter, M.; Span, R. Integration of sorption kinetics in carbon conversion modeling for the description of oxyfuel combustion processes. *Energy Procedia* **2017**, *142*, 1361−1366.

(15) Hao, W.; Björkman, E.; Lilliestråle, M.; Hedin, N. Activated carbons prepared from hydrothermally carbonized waste biomass used as adsorbents for CO2. *Appl. Energy* **2013**, *112*, 526−532.

(16) Islam, M. A.; Ahmed, M. J.; Khanday, W. A.; Asif, M.; Hameed, B. H. Mesoporous activated coconut shell-derived hydrochar prepared via hydrothermal carbonization-NaOH activation for methylene blue adsorption. *J. Environ. Manage.* **2017**, *203*, 237−244.

(17) Sevilla, M.; Maciá-Agulló, J. A.; Fuertes, A. B. Hydrothermal carbonization of biomass as a route for the sequestration of CO2: Chemical and structural properties of the carbonized products. *Biomass Bioenergy* **2011**, *35*, 3152−3159.

(18) Sun, K.; Ro, K.; Guo, M.; Novak, J.; Mashayekhi, H.; Xing, B. Sorption of bisphenol A, 17α-ethinyl estradiol and phenanthrene on thermally and hydrothermally produced biochars. *Bioresour. Technol.* **2011**, *102*, 5757−5763.

(19) Yang, G.; Song, S.; Li, J.; Tang, Z.; Ye, J.; Yang, J. Preparation and CO2 adsorption properties of porous carbon by hydrothermal carbonization of tree leaves. *J. Mater. Sci. Technol.* **2019**, *35*, 875−884.

(20) Yu, J.; Zhu, Z.; Zhang, H.; Chen, T.; Qiu, Y.; Xu, Z.; Yin, D. Efficient removal of several estrogens in water by Fe-hydrochar composite and related interactive effect mechanism of H2O2 and iron with persistent free radicals from hydrochar of pinewood. *Sci. Total Environ.* **2019**, *658*, 1013−1022.

(21) Lei, Y.; Su, H.; Tian, F. A Novel Nitrogen Enriched Hydrochar Adsorbents Derived from Salix Biomass for Cr (VI) Adsorption. *Sci. Rep.* **2018**, *8*, No. 4040.

(22) Lotz, K.; Wütscher, A.; Düdder, H.; Berger, C. M.; Russo, C.; Mukherjee, K.; Schwaab, G.; Havenith, M.; Muhler, M. Tuning the Properties of Iron-Doped Porous Graphitic Carbon Synthesized by Hydrothermal Carbonization of Cellulose and Subsequent Pyrolysis. *ACS Omega* **2019**, *4*, 4448−4460.

(23) Dubinin, M. M.; Astakhov, V. A. Development of the concepts of volume filling of micropores in the adsorption of gases and vapors by microporous adsorbents: Communication 1. Carbon adsorbents. *Russ. Chem. Bull.* **1971**, *20*, 3−7.

(24) Medek, J. Possibility of micropore analysis of coal and coke from the carbon dioxide isotherm. *Fuel* **1977**, *56*, 131−133.

(25) Henrich, E.; Bürkle, S.; Meza-Renken, Z. I.; Rumpel, S. Combustion and gasification kinetics of pyrolysis chars from waste and biomass. *J. Anal. Appl. Pyrolysis* **1999**, *49*, 221−241.

(26) Qian, L.; Zhao, Y.; Sun, S.; Che, H.; Chen, H.; Wang, D. Chemical/physical properties of char during devolatilization in inert and reducing conditions. *Fuel Process. Technol.* **2014**, *118*, 327−334.

(27) Wedler, C.; Arami-Niya, A.; Xiao, G.; Span, R.; May, E. F.; Richter, M. Gas Diffusion and Sorption in Carbon Conversion. *Energy Procedia* **2019**, *158*, 1792−1797.

(28) Himeno, S.; Komatsu, T.; Fujita, S. High-Pressure Adsorption Equilibria of Methane and Carbon Dioxide on Several Activated Carbons. *J. Chem. Eng. Data* **2005**, *50*, 369−376.

(29) An, F.-H.; Cheng, Y.-P.; Wu, D.-M.; Wang, L. The effect of small micropores on methane adsorption of coals from Northern China. *Adsorption* **2013**, *19*, 83−90.

(30) Borchardt-Ott, W.*Crystallography: An Introduction*; Springer-Verlag: Berlin, Heidelberg, 2012.

(31) Zazza, C.; Rutigliano, M.; Sanna, N.; Barone, V.; Cacciatore, M. Oxygen adsorption on β-quartz model surfaces: some insights from density functional theory calculations and semiclassical time-dependent dynamics. *J. Phys. Chem. A* **2012**, *116*, 1975−1983.
(32) Düdder, H.; Wütscher, A.; Stoll, R.; Muhler, M. Synthesis and characterization of lignite-like fuels obtained by hydrothermal carbonization of cellulose. *Fuel* **2016**, *171*, 54−58.
(33) Brunauer, S.; Emmett, P. H.; Teller, E. Adsorption of gases in multimolecular layers. *J. Am. Chem. Soc.* **1938**, *60*, 309−319.
(34) Thommes, M.; Kaneko, K.; Neimark, A. V.; Olivier, J. P.; Rodriguez-Reinoso, F.; Rouquerol, J.; Sing, K. S. W. Physisorption of gases, with special reference to the evaluation of surface area and pore size distribution (IUPAC Technical Report). *Pure Appl. Chem.* **2015**, *87*, 1051−1069.
(35) Garrido, J.; Linares-Solano, A.; Martin-Martinez, J. M.; Molina-Sabio, M.; Rodriguez-Reinoso, F.; Torregrosa, R. Use of nitrogen vs. carbon dioxide in the characterization of activated carbons. *Langmuir* **1987**, *3*, 76−81.
(36) Span, R.; Wagner, W. A New Equation of State for Carbon Dioxide Covering the Fluid Region from the Triple-Point Temperature to 1100 K at Pressures up to 800 MPa. *J. Phys. Chem. Ref. Data* **1996**, *25*, 1509−1596.
(37) Jagiello, J.; Olivier, J. P. Carbon slit pore model incorporating surface energetical heterogeneity and geometrical corrugation. *Adsorption* **2013**, *19*, 777−783.
(38) Jagiello, J.; Olivier, J. P. 2D-NLDFT adsorption models for carbon slit-shaped pores with surface energetical heterogeneity and geometrical corrugation. *Carbon* **2013**, *55*, 70−80.
(39) Jensen, N. K.; Rufford, T. E.; Watson, G.; Zhang, D. K.; Chan, K. I.; May, E. F. Screening Zeolites for Gas Separation Applications Involving Methane, Nitrogen, and Carbon Dioxide. *J. Chem. Eng. Data* **2012**, *57*, 106−113.
(40) Li, G. K.; Shang, J.; Gu, Q.; Awati, R. V.; Jensen, N.; Grant, A.; Zhang, X.; Sholl, D. S.; Liu, J. Z.; Webley, P. A.; et al. Temperature-regulated guest admission and release in microporous materials. *Nat. Commun.* **2017**, *8*, No. 15777.
(41) Rufford, T. E.; Watson, G. C. Y.; Saleman, T. L.; Hofman, P. S.; Jensen, N. K.; May, E. F. Adsorption Equilibria and Kinetics of Methane + Nitrogen Mixtures on the Activated Carbon Norit RB3. *Ind. Eng. Chem. Res.* **2013**, *52*, 14270−14281.
(42) Watson, G. C.; Jensen, N. K.; Rufford, T. E.; Chan, K. I.; May, E. F. Volumetric Adsorption Measurements of N 2, CO 2, CH 4, and a CO 2 + CH 4 Mixture on a Natural Chabazite from (5 to 3000) kPa. *J. Chem. Eng. Data* **2012**, *57*, 93−101.
(43) Xiao, G.; Li, Z.; Saleman, T. L.; May, E. F. Adsorption equilibria and kinetics of CH4 and N2 on commercial zeolites and carbons. *Adsorption* **2017**, *23*, 131−147.
(44) Venkatraman, A.; Fan, L. T.; Walawender, W. P. Nonideality Correction Factors for Adsorbates. *J. Colloid Interface Sci.* **1996**, *183*, 291−294.
(45) Hallmann, S.; Fink, M. J.; Mitchell, B. S. Wetting properties of silicon films from alkyl-passivated particles produced by mechanochemical synthesis. *J. Colloid Interface Sci.* **2010**, *348*, 634−641.
(46) Shaikh, R. P.; Pillay, V.; Choonara, Y. E.; Du Toit, L. C.; Ndesendo, V. M. K.; Kumar, P.; Khan, R. A. The application of a crosslinked pectin-based wafer matrix for gradual buccal drug delivery. *J. Biomed. Mater. Res., Part B* **2012**, *100*, 1029−1043.
(47) Emmett, P. H.; Brunauer, S. The Use of Low Temperature van der Waals Adsorption Isotherms in Determining the Surface Area of Iron Synthetic Ammonia Catalysts. *J. Am. Chem. Soc.* **1937**, *59*, 1553−1564.
(48) Ortiz-Vega, D. O.; Hall, K. R.; Holste, J. C.; Arp, V. D.; Harvey, A. H.; Lemmon, E. W.Helmholtz equation of state for helium*J. Phys. Chem. Ref. Data*; 2020.
(49) Setzmann, U.; Wagner, W. A New Equation of State and Tables of Thermodynamic Properties for Methane Covering the Range from the Melting Line to 625 K at Pressures up to 100 MPa. *J. Phys. Chem. Ref. Data* **1991**, *20*, 1061−1155.
(50) Stewart, R. B.; Jacobsen, R. T.; Wagner, W. Thermodynamic Properties of Oxygen from the Triple Point to 300 K with Pressures to 80 MPa. *J. Phys. Chem. Ref. Data* **1991**, *20*, 917−1021.
(51) Span, R.; Lemmon, E. W.; Jacobsen, R. T.; Wagner, W.; Yokozeki, A. A Reference Equation of State for the Thermodynamic Properties of Nitrogen for Temperatures from 63.151 to 1000 K and Pressures to 2200 MPa. *J. Phys. Chem. Ref. Data* **2000**, *29*, 1361−1433.
(52) Span, R.; Beckmüller, R.; Eckermann, T.; Herrig, S.; Hielscher, S.; Jäger, A.; Mickoleit, E.; Neumann, T.; Pohl, S.; Semrau, B.; et al.*TREND: Thermodynamic Reference and Engineering Data*; Lehrstuhl für Thermodynamik, Ruhr-Universität Bochum, 2019.
(53) International Organization for Standardization. *Uncertainty of Measurement—Part 3: Guide to the Expression of Uncertainty in Measurement*; ISO: Geneva, 2008.

https://dx.doi.org/10.1021/acsomega.9b04370
ACS Omega 2020, 5, 10704−10714